Received: 15 June 2022 | Revised: 26 August 2022 | Accepted: 14 September 2022 | Published on: 13 October 2022

DOI: 10.1002/mrm.29477

RESEARCH ARTICLE

Magnetic Resonance in Medicine

Noninvasively differentiating acute and chronic nephropathies via multiparametric urea-CEST, nuclear Overhauser enhancement-CEST, and quantitative magnetization transfer MRI

Soo Hyun Shin[1] | **Michael F. Wendland**[2] | **Jingshen Wang**[3] | **Mark Velasquez**[1] | **Moriel H. Vandsburger**[1]

[1]Department of Bioengineering, University of California, Berkeley, Berkeley, California, USA

[2]Berkeley Preclinical Imaging Core (BPIC), University of California, Berkeley, Berkeley, California, USA

[3]Department of Biostatistics, University of California, Berkeley, Berkeley, California, USA

Correspondence
Moriel H. Vandsburger, Department of Bioengineering, University of California, Berkeley 281 Hearst Memorial Mining Building Berkeley, CA 94720, USA.
Email: moriel@berkeley.edu

Funding information
American Heart Association (AHA), Grant/Award Number: 19TPA34850040; National Institutes of Health (NIH), Grant/Award Numbers: 1R01HL28592, UH2EB028908, UH3EB028908

Purpose: Standardized blood tests often lack adequate sensitivity and specificity to capture the gradual progression of renal injuries. We suggest a multiparametric molecular MRI approach as a noninvasive tool for monitoring renal function loss and distinguishing different types of renal injuries.

Methods: CEST and quantitative magnetization transfer (qMT) imaging were performed on cisplatin ($n = 16$) and aristolochic acid (AA)-induced nephropathy ($n = 22$) mouse models at 7T with an infusion of either saline or urea. Seven-pool Lorentzian fitting was applied for the analysis of CEST Z-spectra, and the T_1-corrected CEST contrast apparent exchange-dependent relaxation (AREX) from urea (+1 ppm) and two nuclear Overhauser enhancement (NOE) pools (−1.6 and −3.5 ppm) were measured. Similarly, qMT spectra were fitted into two-pool Ramani equation and the relative semi-solid macromolecular pool-size ratio was measured. Histology of mouse kidneys was performed to validate the MR findings.

Results: AA model showed disrupted spatial gradients of urea in the kidney and significantly decreased NOE CEST and qMT contrast. The cisplatin model showed slightly decreased qMT contrast only. The orrelation of MR parameters to histological features showed that NOE CEST and qMT imaging are sensitive to both acute and chronic injuries, whereas urea CEST shows a significant correlation only to acute injuries.

Conclusion: These results indicate that our multiparametric approach allows comprehensive and totally noninvasive monitoring of renal function and histological changes for distinguishing different nephropathies.

KEYWORDS
CEST, kidney, MRI, NOE, qMT imaging, urea

1 | INTRODUCTION

Standardized blood tests such as serum creatinine level (SCr) and blood urea nitrogen (BUN) are widely used for the diagnosis of renal diseases.[1,2] Although these tests are effective in measuring the renal function represented by the estimated glomerular filtration rate (eGFR), the hyperfiltration by intact nephrons often hinders the detection of renal functional decline until 50% of the function is lost.[3] This late detection of renal function loss is critical especially in clinical scenarios that accompany the gradual progression of renal function loss after an acute injury, such as acute kidney injury (AKI)-to-chronic kidney disease (CKD) transition and delayed graft rejection after renal transplant.[4,5] Because the gradual loss in renal function is often not picked up by blood tests, there is currently no reliable method other than biopsy to detect such subtle damages in the kidneys in a timely manner.[6,7] The incidence of acute injuries often elevates the risk of an additional episode of acute injuries, requiring follow-up monitoring of pathological status of the kidney to track and distinguish progression to CKD and an incidence of AKI.[8]

Medical imaging can aid such repeated monitoring of the kidney in a noninvasive manner. Currently, however, medical imaging modalities such as ultrasound, CT, and MRI are mostly limited to detecting structural abnormalities such as the size of the kidney, cysts, and tumors.[9–12] Functional imaging methods such as Doppler ultrasound and contrast-enhanced CT and MRI are focused on perfusion only and do not report parenchymal injuries.[13,14] More importantly, contrast agents used for CT and MRI perfusion imaging are contraindicated to renal disease patients and may induce nephrogenic systemic fibrosis.[15,16] Therefore, a noninvasive imaging method that directly and comprehensively reports renal function and underlying tissue alterations is urgently needed.

CEST imaging is a novel molecular MRI technique that generates contrast from a molecule of interest by using radiofrequency saturation at the offset frequencies of exchangeable protons on the molecule of interest to label the magnetic moment and bias the subsequent signal intensity as a function of chemical exchange.[17–19] Recently, we demonstrated the feasibility of quantitative imaging of urea in healthy mouse kidneys using CEST MRI.[20,21] Similarly, others have demonstrated the ability to monitor renal pH using CEST MRI contrast agents.[22–25] Urea is a major component of the spatial osmolarity gradient in the kidney through which fine tuning of water reabsorption is achieved.[26–28] As previous mouse studies have shown disrupted urea gradients in the kidney on the onset of sepsis-induced AKI and diabetic nephropathy, we hypothesized that the aforementioned urea CEST MRI method can be a useful tool for noninvasively monitoring the progression of renal diseases.[29,30]

Renal injuries often involve various cellular and molecular level alterations, such as tubular cell necrosis, apoptosis, and fibrosis development. These diverse patterns of renal injuries may not be accurately captured by a single urea CEST contrast and require other MR parameters that reflect different characteristics of the injury. Because CEST MRI is performed by saturating multiple offset frequencies around the resonant frequency of water, CEST contrast from other exchangeable protons can be harnessed simultaneously for a thorough investigation of renal pathology. For instance, CEST contrast from aliphatic and olefinic protons generated via relayed nuclear Overhauser enhancement (NOE) is widely studied for imaging brain tumors and infarction from ischemia.[31,32] The NOE CEST contrast has also shown the potential of detecting nephropathies in a mouse study.[33,34] Similarly, quantitative magnetization transfer (qMT) contrast from semisolid macromolecules can also be achieved by targeting far offset frequencies and extracting the relative pool-size ratio (PSR) of the bound water pool.[35,36] This method has shown to be sensitive to fibrosis, a hallmark of CKD, in multiple preclinical renal studies.[37,38] Overall, these methods may complement urea CEST MRI by providing different aspects of renal pathology, allowing comprehensive investigation of renal function and tissue integrity.

In this study, we demonstrate a multiparametric CEST and qMT approach for noninvasively monitoring renal disease progression. We used cisplatin and aristolochic acid (AA) to induce two distinct nephropathies in mice to examine whether our approach can capture distinct characteristics of each model and differentiate them. Multiparametric imaging results were correlated to histological analyses to pursue the pathological origin of CEST and qMT contrast changes.

2 | METHODS

2.1 | Mouse renal disease models

All animal experiments were performed in accordance with the Institutional Animal Care and Use Committee guidelines. Cisplatin (Fresenius Kabi) was used for inducing chronic and mild renal injuries, and AA (Acros Organics) for acute and severe renal injuries. For the cisplatin group, 10- to 12-week-old male C57BL6/J mice (n = 26) were intraperitoneally injected with 10 mg/bw kg of cisplatin every week from week 0 to 3. Blood was collected every week for the measurement of BUN and SCr (n = 10). The other mice (n = 16) were scanned

every week up to week 4. Mice were intraperitoneally infused with either 150 μL saline ($n = 8$) or 2 M 150 μL urea ($n = 8$) during each scan to see renal response via urea CEST.

For the AA model, mice of the same age and species ($n = 32$) were i.p. injected with 5 mg/b.w. kg of AA dissolved in polyethylene glycol (Acros Organics) every day from day 0 to 4. Blood collection ($n = 10$) for BUN and SCr measurement and MR scans with saline ($n = 10$) or urea ($n = 12$) infusion were performed at days 0 and 5.

2.2 | In vivo MRI acquisition

MR scans were performed at 7T with a 40 mm volume coil (Bruker PharmaScan). To tightly control diuretic states, every MR scan was initiated at ZT0 (7 AM) after 12-hour fasting. T_2-weighted images (RARE factor = 8, TR/TE = 2500/52 ms, number of average = 2, slice thickness = 2 mm, FOV = 35 × 35 mm, matrix = 256 × 256), T_1 maps (inversion recovery, TR/TE = 4.3/2.1 ms per k-space line, 15 TIs from 100 to 8000 ms, matrix = 128 × 128), CEST Z-spectra (TR/TE = 7.4/3.1 ms per k-space line, number of average = 2, 59 offset frequencies, 70 0.6 μT 50-ms Gaussian sat pulses with duty cycle = 50%, matrix = 128 × 128, 5 s recovery time) were acquired before and 20 min after the infusion of saline or urea. Each CEST Z-spectrum was acquired in a linear fashion from positive to negative offset frequencies. During the acquisition of CEST Z-spectra, reference images (−300 ppm offset) were acquired every 5 offset images for retrospective thermal drift correction.[32,39] B_0 and B_1 maps were acquired via water shift and B_1 (WASABI) method (3.7 μT, 5 ms-long block pulse, the same readout as CEST, 41 offset frequencies from −2 to 2 ppm), and MT-weighted images (FLASH, TR/TE = 24/2.5 ms, flip angle = 7°, number of average = 24) at two saturation powers (flip angle = 220° and 820°, 10 ms Gaussian pulse) with seven offset frequencies each (1, 2.5, 5, 8.5, 15, 35, and 80 kHz) were also acquired for qMT measurements.

2.3 | CEST and qMT data analysis

All MR data analysis was performed by a custom-written code in MATLAB (The Mathworks). B_0 inhomogeneity was corrected voxel-wise using B_0 maps acquired from WASABI. Because B_1 maps showed minimal inhomogeneity, no B_1 correction was needed. After corrections, kidneys were segmented into the cortex, outer medulla (OM) and inner medulla and papilla (IM + P) by drawing region-of-interests (ROI) on T_2-weighted images and applying to CEST and qMT-weighted images. Using reference images that were periodically acquired during Z-spectra acquisition, thermal drift was corrected by spline interpolation. Offset images showing severe motion artifacts were excluded from the analysis. ROI-averaged CEST Z-spectra were fitted to seven-pool (water, MT, amine, amide, urea, NOE at −1.6 ppm, and NOE at −3.5 ppm) Lorentzian functions as previously described.[21] After fitting to the sum of Lorentzian functions, the apparent exchange-dependent relaxation (AREX) method was applied to measure the T_1-corrected CEST contrast, which was used for all CEST contrast measurements.[40] Voxel-wise qMT spectra were fitted to a two-pool Ramani equation to derive the PSR, the ratio of semi-solid macromolecule pool to free water pool.[41]

2.4 | Histology analysis

Renal injuries were evaluated on paraffin-embedded sections with hematoxylin/eosin and Sirius red staining. Lesions were classified according to an adaptation of a previously published criterion and scored according to a 5-tier severity scale.[42] Tubular necrosis, atrophy, degeneration, and dilation: 0, normal; 1, minimal (<10% of tubules affected); 2, mild (10%–30% of tubules affected); 3, moderate (30%–60% of tubules affected); 4: marked (more than 60% of tubules affected). Fibrosis: 0, normal; 1, minimal (uncommon detection in <10% kidney fields 200×); 2, mild (detectable in up to 30% of kidney fields); 3, moderate (detectable in up to 30%–60% of kidney fields); 4, marked (detectable in more than 60% of kidney fields). A final cumulative layout shift score was created by the sum of tubular necrosis, atrophy, and fibrosis.

2.5 | Statistical analysis

All statistical analyses were performed using GraphPad Prism 9 (GraphPad Software). The normality of the data was confirmed by the Shapiro–Wilk test. BUN and SCr measurements were compared using one-way ANOVA for the cisplatin group and paired *t*-test for the AA group. Mixed-model effects analysis with Sidak's post hoc test was performed for comparing MR measurements. Kruskal-Wallis test with Dunn's multiple comparison test was used for analyzing histological scores, and Spearman's rank correlation coefficient was used for measuring the association between MR parameters and histological scores.

3 | RESULTS

3.1 | Validating cisplatin and AA nephropathy models by blood tests

To confirm the development of renal injuries from cisplatin and AA administration, BUN and SCr were measured over time from mice. Blood tests showed significant increases in BUN and SCr in both the cisplatin and AA groups (Figure 1). The BUN of the cisplatin group significantly increased at week 2 compared to week 0 (23.55 ± 2.50 to 39.38 ± 11.01 mg/dL; $p = 0.0032$), and an increase in SCr was evident at week 3 (0.115 ± 0.049 to 0.242 ± 0.119 mg/dL, $p = 0.0326$). The AA group showed substantial increases of both BUN (27.31 ± 6.62 to 64.44 ± 12.86 mg/dL, $p = 0.0008$) and SCr (0.12 ± 0.07 to 1.64 ± 1.27 mg/dL, $p = 0.0074$) 5 days after the initiation of AA injections. Overall, blood tests indicated the progression of renal injuries in both cisplatin and the AA group, but the extent of renal function loss was more severe in the AA group.

3.2 | In vivo CEST and qMT MRI scans of cisplatin and AA nephropathy models

After the disease models were validated by blood tests, the mice from the two disease models were scanned with MRI to quantify T_1 relaxation times, acquire CEST Z-spectra, and measure the pool-size ratio by qMT. Each series of acquisitions was performed twice per scan, before and after the infusion of either 150 μL of saline or 2 M urea, to observe the renal response to the infusion as a change of urea CEST. Both models showed significant increases in T_1 times in the cortex (Figure 2). The cisplatin group showed increased T_1 times in the cortex at week 1 compared to the baseline (1182 ± 34 to 1292 ± 80 ms, $p = 0.0011$), which was sustained up to week 3 (1276 ms, $p = 0.0009$) (Figure 2C). Similar changes were transiently observed in the OM at week 1 (1455 ± 70 to 1523 ± 85 ms, $p = 0.0399$). In contrast, the AA group showed larger increases in T_1 values at day 5 in the cortex (1207 ± 56 to 1516 ± 94 ms, $p < 0.0001$) as shown in the representative T_1 maps (Figure 2B).

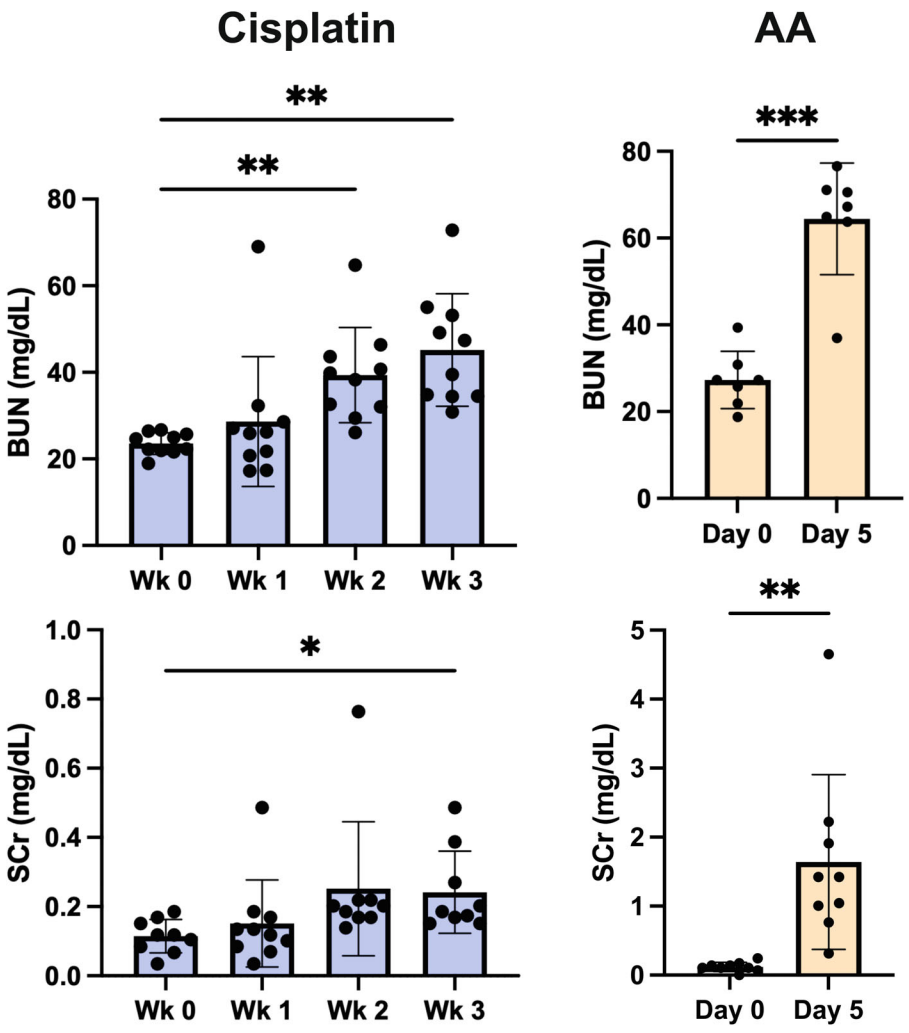

FIGURE 1 Blood tests for cisplatin and aristolochic acid (AA)-induced nephropathy models. The cisplatin group shows a steady increase of both blood urea nitrogen (BUN) and serum creatinine (SCr) level. BUN starts showing a significantly higher level than the week 0 baseline from week 2, and SCr from week 3, indicating chronic development of renal injuries. AA group shows more acute and severe development of renal injuries reflected by a much more significant increase of both BUN and SCr in 5 days. *$p < 0.05$, **$p < 0.01$, ***$p < 0.001$

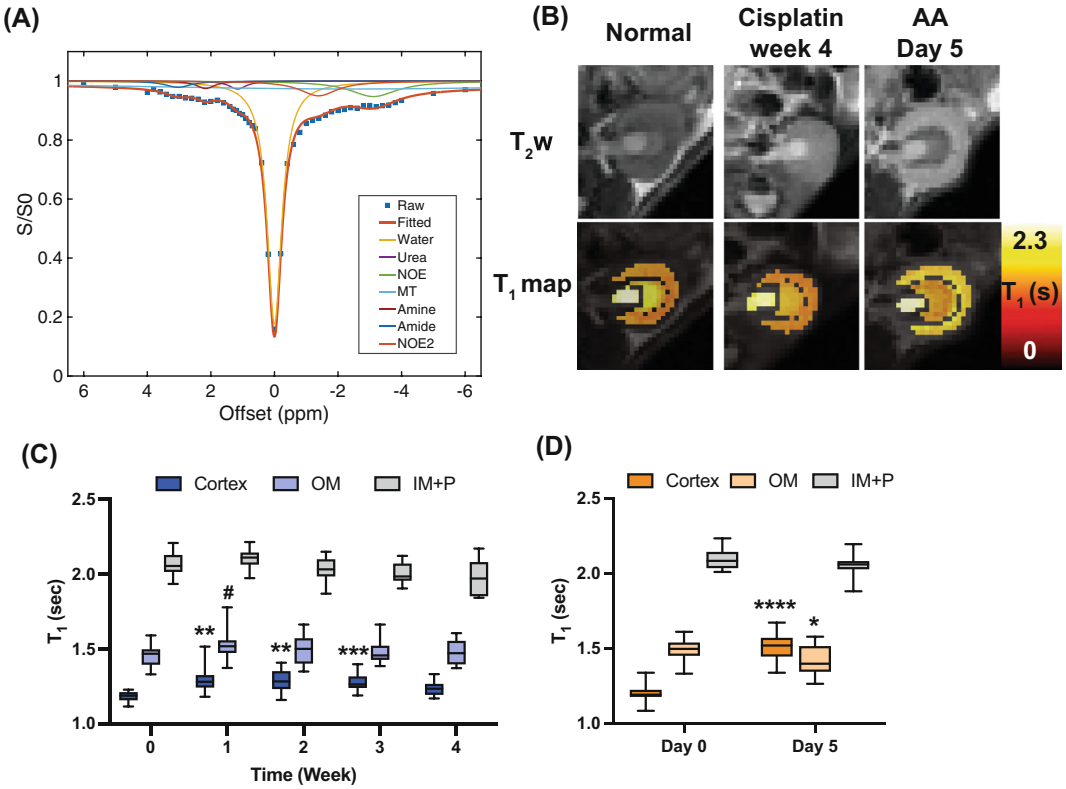

FIGURE 2 In vivo multi-parametric MRI results. (A) A representative Z-spectrum derived from a series of CEST-MR images and localized to the mouse cortex is analyzed via seven-pool Lorentzian fitting. Urea contrast at 1 ppm, nuclear Overhauser enhancement (NOE) contrast at −1.6 ppm, and NOE contrast at −3.5 ppm are indicated by a solid arrow, dashed arrow, and dotted arrow, respectively. (B) Representative T_2-weighted (T_2w) anatomical images and T_1 maps of cisplatin and aristolochic acid (AA) nephropathy models reveal structural and parametric changes induced by kidney injury. The AA group showed reversed contrast in the cortex and the outer medulla in T_2w images and increased T_1 times in the cortex as a function of injury, likely because of the expansion of the free water pool by tubular dilation. In parallel, T_1 times in the cortex and outer medulla increased significantly in both the cisplatin group (C) and the AA group (D) despite different manifestations of kidney injury. $^{*\#}p < 0.05$, $^{**}p < 0.01$, $^{***}p < 0.001$, $^{****}p < 0.0001$ vs. week/day 0

For the measurement of CEST contrast from urea, the CEST contrast at 1 ppm was corrected for T_1 times based on the AREX method (Figure 2A).[40] The pre-infusion spatial gradient of urea AREX contrast was measured by normalizing the urea AREX from the OM and inner medulla and papilla (IM + P) to that from the cortex (Figure 3A). The endogenous spatial gradient of urea AREX did not change over time in the cisplatin group, whereas the AA group showed significant increases of the OM-to-cortex urea AREX ratio as a function of disease progression. The ratio increased from 0.511 ± 0.116 to 0.773 ± 0.215 ($p = 0.0003$) in the urea-infused subgroup. Similarly, the ratio increased from 0.531 ± 0.124 to 0.843 ± 0.141 ($p = 0.0001$) in the saline-infused group. This trend of a disrupted urea AREX gradient between the OM and the cortex is observed in the urea AREX maps overlaid on T_2-weighted anatomical images (Figure 3B).

The renal response to the infusion of either urea or saline was further assessed by measuring the fold change of urea AREX contrast following infusion of either saline or urea (Figure 3C). The fold change of urea AREX contrast, either with an infusion of saline or urea, did not change over injury progression in the cisplatin group. The AA group, on the other hand, showed a decreased response in the cortex (1.433 ± 0.456 to 0.993 ± 0.319, $p = 0.039$) and the OM (1.556 ± 0.406 to 0.951 ± 0.337, $p = 0.0055$) compared to the baseline measurement. The saline infusion did not cause any changes in urea AREX contrast in both healthy and injured conditions.

On top of urea CEST, NOE CEST contrasts at −3.5 ppm and −1.6 ppm were also recorded from the full Z-spectra and corrected for T_1 times via AREX (Figure 4). Similar to urea AREX results, the cisplatin group did not show significant changes in NOE contrasts at both −3.5 ppm and −1.6 ppm over time. The AA group showed significant decrease of NOE AREX at −3.5 ppm (0.104 ± 0.014 to 0.076 ± 0.012, $p < 0.0001$) and −1.6 ppm (0.096 ± 0.021 to 0.072 ± 0.011, $p = 0.0001$) in the cortex (Figure 4A). NOE AREX was preserved in other regions of the kidney. NOE AREX maps also show a significant decrease of contrast

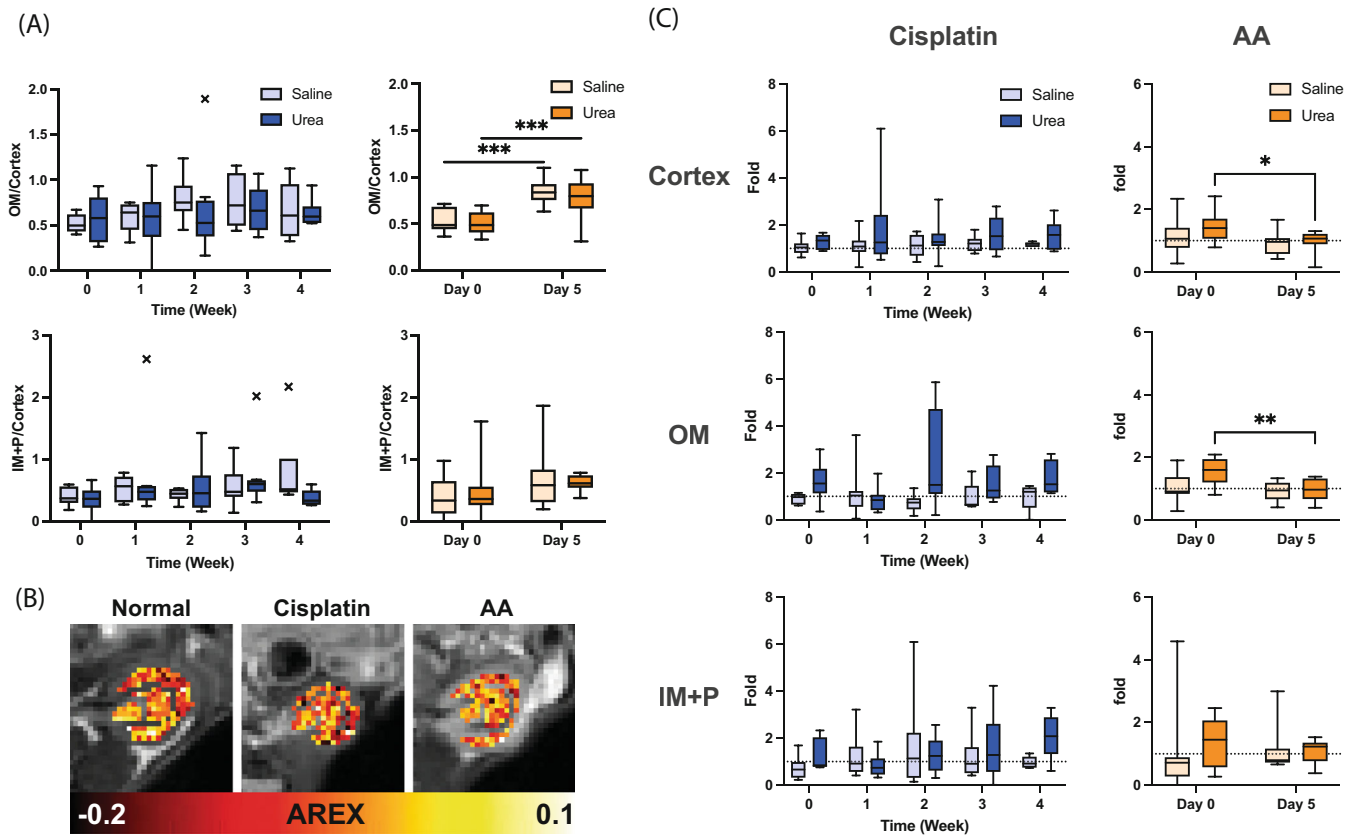

FIGURE 3 Urea CEST contrast measurements. (A) The pre-infusion spatial gradient of urea contrast was calculated by normalizing pre-infusion apparent exchange-dependent relaxation (AREX) measurements at the outer medulla (OM) and the inner medulla and papilla (IM + P) to the corresponding measurements at the cortex. Measurements of the spatial gradient of urea AREX in the cisplatin group showed no changes over time, whereas the aristolochic acid (AA) group showed a significant increase of normalized OM contrast from both saline and urea-infused subgroups. "x" marks represent outliers. ***$p < 0.001$. (B) Representative urea AREX maps of normal and diseased kidneys show preserved urea AREX contrast in the cisplatin group, whereas the AA group shows increased contrast in the OM, resulting in the decrease of contrast gradient between the cortex and OM. (C) The fold change of urea AREX on the infusion of either saline or urea was calculated by dividing the post-infusion urea AREX measurement by the pre-infusion measurement. The kidney response to urea or saline infusion did not change in the cisplatin group, whereas the AA group shows decreased fold change on urea infusion in the cortex and OM at day 5. *$p < 0.05$, **$p < 0.01$

in the AA group, whereas no change is observed from the cisplatin group (Figure 4B).

Finally, qMT spectra were acquired at two saturation powers with seven offset frequencies each and fitted to Ramani equation to extract a semi-solid macromolecular PSR (Figure 5A).[41] In this study, the cisplatin group showed slight decreases of PSR in the cortex at weeks 2 (0.045 ± 0.005, $p = 0.0481$) and 3 ($0.04c \pm 0.005$, $p = 0.0386$) compared to baseline measurements at week 0 (0.05 ± 0.005) (Figure 5C). Much more significant decreases of PSR were detected from the AA group on injury initiation in the cortex (0.047 ± 0.003 to 0.032 ± 0.005, $p < 0.0001$) (Figure 5D). Both groups did not show any changes of PSR in other regions of the kidney. This trend of PSR decrease is again well represented in the qMT contrast maps shown in Figure 5B.

3.3 | Comparing CEST and qMT parameters to histological analysis

After in vivo MR scans were complete the mice were euthanized, and the kidneys were collected for histological analysis. Hematoxylin and eosin staining showed marked tubular necrosis in the AA group and moderate areas of tubular atrophy in the cisplatin group (Figure 6A). Sirius red staining revealed interstitial fibrosis in the cisplatin group, whereas the AA group did not show significant changes in collagen content. Semi-quantitative histological scores also showed significantly larger extents of acute injuries, such as tubular necrosis (3.75 ± 0.87 vs. 1.00 ± 0.43, $p = 0.001$), degeneration (3.50 ± 0.90 vs. 1.50 ± 0.90, $p = 0.0017$), and dilation (3.67 ± 0.89 vs. 2.00 ± 0.74, $p = 0.0038$) in the AA group compared

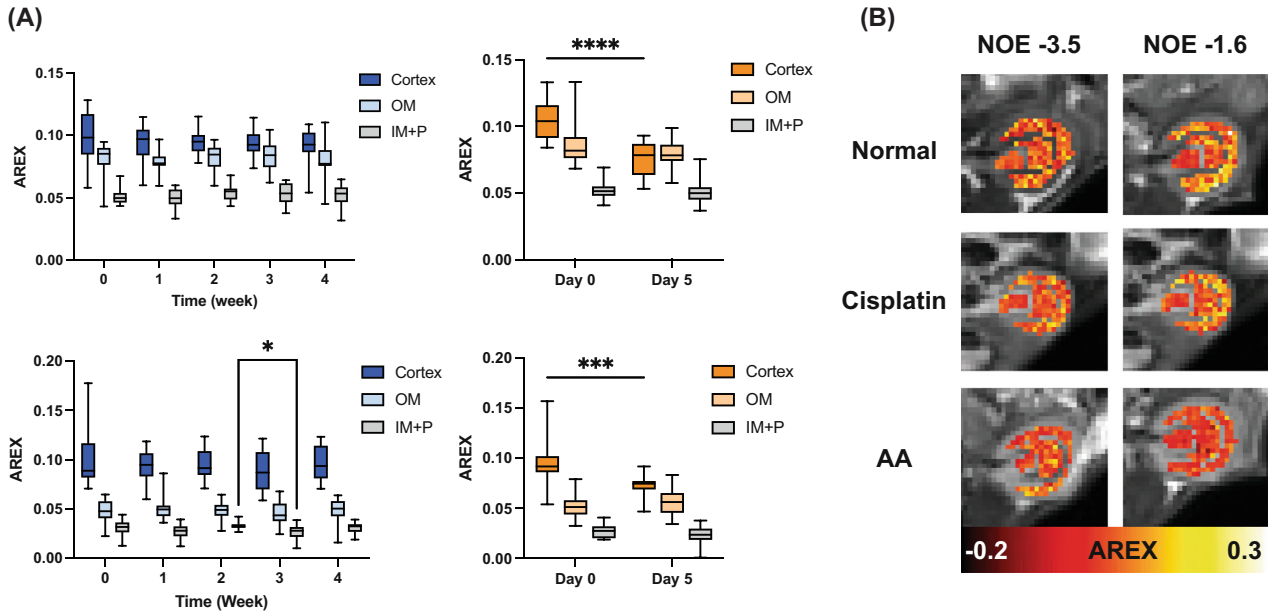

FIGURE 4 Nuclear Overhauser enhancement (NOE) CEST contrast measurements. (A) NOE apparent exchange-dependent relaxation (AREX) measurements at −3.5 and −1.6 ppm offset frequencies show no or little changes in the NOE contrast in the cisplatin group. The aristolochic acid (AA) group, however, shows a significant decrease of contrast in the cortex at both −3.5 and −1.6 ppm, possibly because of the disruption of cellular membranes and alterations in mobile proteins. *$p < 0.05$, ***$p < 0.001$, ****$p < 0.0001$. (B) NOE AREX maps overlaid on T_2-weighted images. AA group shows a significant decrease of the contrast at both −3.5 and −1.6 ppm in the cortex compared to the normal mice.

to the cisplatin group (Figure 6B). Chronic features of renal injuries such as tubular atrophy (1.92 ± 0.79 vs. 0.42 ± 0.51, $p = 0.001$) and interstitial fibrosis (1.50 ± 0.52 vs. 0.25 ± 0.45, $p = 0.0002$) were significantly more evident in the cisplatin group than the AA group. These histological scores were correlated with MR parameters that showed significant changes in disease progression (Figure 7). Spearman rank correlation showed that PSR and NOE AREX at −1.6 ppm are negatively related to acute injuries and positively related to chronic injuries. The T_1 time in the cortex also showed a significant correlation to all the histological features, but in the opposite fashion: positively correlated to acute injuries and negatively correlated to chronic injuries. Urea AREX at the OM and NOE AREX at −3.5 ppm were only sensitive to acute injuries. As a visual representation of how multiparametric analysis can distinguish acute and chronic injuries, mouse histology data were clustered based on T_1, PSR, and urea AREX (Figure 7C). This clustering demonstrates that a combination of CEST and qMT parameters can clearly distinguish kidneys with acute injuries from those with chronic ones.

4 | DISCUSSION

This study shows that multiparametric CEST MRI and qMT imaging can quantitatively distinguish the differing pathologies of renal injuries induced by cisplatin and AA. Administration of cisplatin and AA yielded vastly different patterns of disease progression as confirmed by blood tests and histology. This difference was well captured by our imaging method as different patterns of changes in urea and NOE CEST and qMT parameters. The relatively mild and chronic injuries induced by cisplatin showed changes only in T_1 times and PSR at the cortex from qMT, whereas the relatively acute and severe injuries shown in the AA model were reflected as significant changes of T_1, PSR, urea, and NOE CEST contrast. Correlation to histological scores revealed that CEST contrasts from urea and NOE at −3.5 ppm are highly sensitive specifically to acute injuries, whereas other parameters were responsive to any type of injuries. These results collectively demonstrate the potential diagnostic value of our multiparametric CEST and qMT approach for noninvasively distinguishing different types of renal injuries and monitoring the progression of renal diseases.

We recently showed the feasibility of in vivo CEST imaging of urea in healthy mouse kidneys and further optimized the method to be more quantitative by correcting for the effects of regionally heterogeneous T_1 times on CEST contrast.[21] In this study, we tested whether this approach has diagnostic use in renal diseases, especially focusing on whether it can distinguish differences between the two nephropathies. Our results show that both endogenous

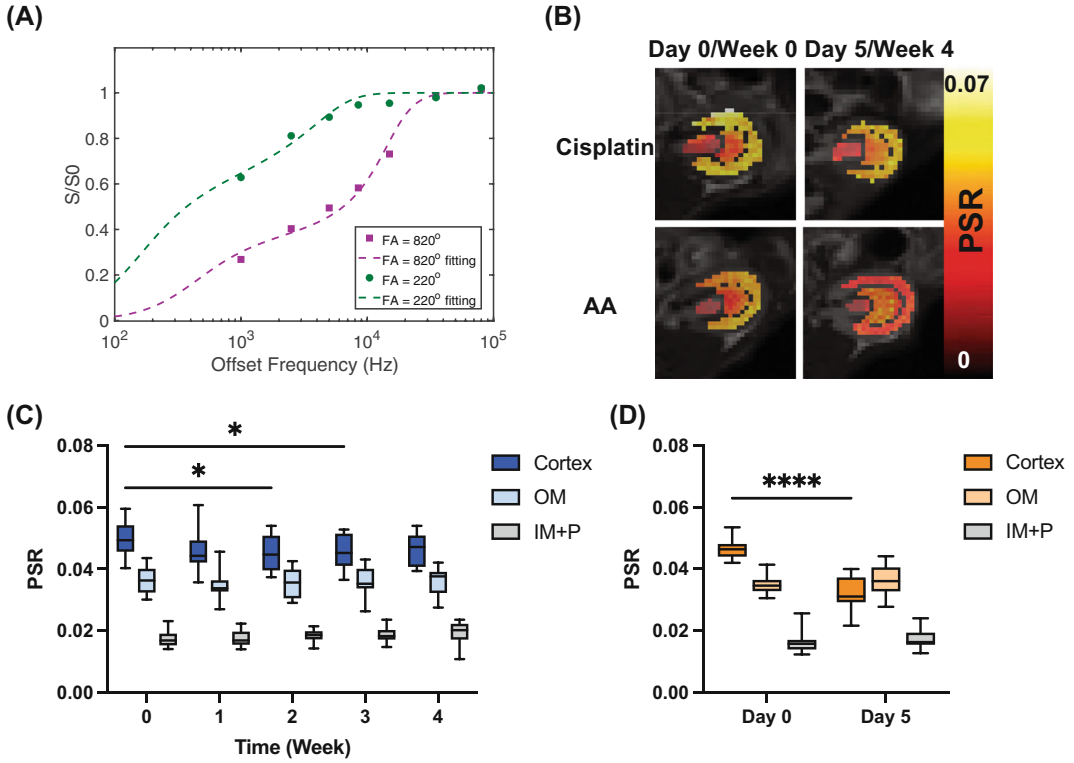

FIGURE 5 Quantitative magnetization transfer (qMT) imaging and pool-size ratio (PSR) measurements. (A) An example qMT spectra acquired at two saturation powers and seven offset frequencies with fitting to the Ramani model. (B) PSR maps of cisplatin and aristolochic acid (AA) group before and after inducing nephropathies. The cisplatin group shows a mild decrease of PSR contrast in the cortex, and the AA group shows a significant decrease in the same region. (C) PSR measurements over time from the cisplatin group show a mild decrease of PSR in the cortex up to week 3, possibly because of the net sum effect of fibrosis development and acute injuries. *$p < 0.05$. (D) PSR measurements from the AA group show a large decrease of PSR in the cortex. Similar to the T_1 increase, this large decrease of PSR may be the consequence of the expansion of the free water pool from tubular injuries and the subsequent decrease of the relative semi-solid macromolecule pool. ****$p < 0.0001$

urea CEST contrast and the CEST response to the infusion of additional urea are sensitive to acute injuries induced by AA, whereas the cisplatin group did not show any changes. The correlation to histological scores also revealed that urea CEST is only sensitive to acute tubular injuries. Considering that the AA model showed significantly larger extents of tubular injuries than the cisplatin group, this observation may be because of the disruption of the urea gradient in the kidney, as a result of acute injuries on tubules on which urea transporters are expressed for urea recycling actions.[27] This is in line with previous studies on hyperpolarized ^{13}C imaging that showed a disrupted urea gradient in a mouse diabetic nephropathy model.[30,43]

On top of urea CEST, NOE CEST and qMT imaging were also performed for a thorough investigation of renal injury progression. It was previously shown that NOE CEST contrast at −3.5 ppm decreases upon the development of sepsis-induced AKI in mice, which was replicated in our results.[33] We also tried to identify the histological origin of the decrease of NOE CEST contrast. Similar to urea CEST, NOE at −3.5 ppm showed a significant correlation only to acute injuries such as tubular necrosis, degeneration, and dilation. This may be because of the decrease in aliphatic and olefinic protons in the tissue caused by disruption of the tubular cell membrane and reduced mitochondrial biogenesis leading to the loss of mobile macromolecules as previously shown.[44,45] The decrease of NOE CEST contrast may also be because of the loss of semi-solid macromolecules, which is supported by the decrease of qMT PSR observed in this study.

PSR from qMT imaging was previously shown to be an indicator of fibrosis development in the mouse and swine kidneys of various disease models including diabetic nephropathy and renal artery stenosis.[37,38,46–48] Similarly, we included a qMT scan protocol in this study to detect any fibrosis development from renal injuries via an increase of PSR. Paradoxically, the PSR measurements decreased in both cisplatin and AA groups, whereas the degree of decrease was much larger in the AA group. Because the AA group showed little or no development of fibrosis while showing severe tubular injuries, the decrease of PSR may arise from the insufficient development of fibrosis with concurrent acute tubular injuries accompanied by the loss of semisolid macromolecules and the expansion

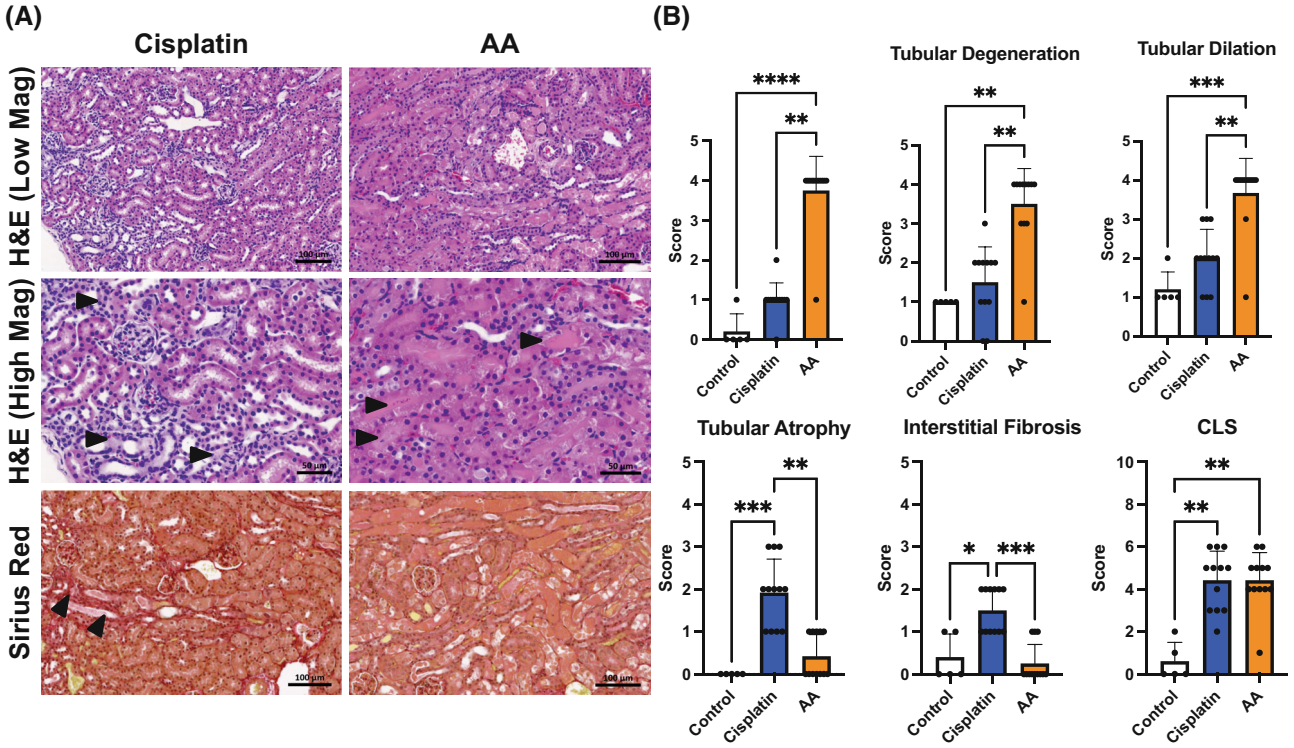

FIGURE 6 Histology and semi-quantitative scoring. (A) Hematoxylin and eosin (H&E) and Sirius red-stained sections of the kidneys. H&E-stained sections from the cisplatin group show multifocal tubular atrophy characterized by peritubular interstitial fibrosis and thickening of the basal lamina (arrowheads). Arrowheads in the Sirius red sections also show focal interstitial fibrosis. H&E staining of the aristolochic acid (AA) group shows marked areas of tubular necrosis, characterized by luminal accumulation of pyknotic cellular debris (arrowheads). No interstitial fibrosis was observed from the Sirius red staining in the case of the AA group. (B) Semi-quantitative scoring of histology. The AA group shows significantly higher scores in tubular necrosis, degeneration, and dilation, which are considered the feature of acute injuries. The cisplatin group shows significantly higher scores from tubular atrophy and interstitial fibrosis, indicating more chronic development of renal injuries. *$p < 0.05$, **$p < 0.01$, ***$p < 0.001$, ****$p < 0.0001$

of the free water pool via tubular dilation. This implies that both acute and chronic injuries alter PSR in either a decreasing or increasing fashion, respectively. Further, the PSR measurements may remain unchanged because of a combination of ongoing acute and chronic injuries. This implication is also supported by the fact that PSR measurements at week 4 in the cisplatin group did not show significant differences from the baseline measurements. As such, the counter-balancing effect of acute and chronic injuries demonstrates that the qMT imaging alone is not sufficient for accurately monitoring the renal tissue status and requires other MR parameters to complement the observations.

NOE contrast measured at −1.6 ppm is a recently discovered CEST contrast.[49] Although the origin of this contrast is largely unexplored, it has been shown that decreased contrast at −1.6 ppm exists in regions of ischemic stroke in rats and has the potential as a new imaging biomarker.[50–53] This novel contrast was also shown to be varying depending on the type of breathing gases for rats, suggesting the possibility that this contrast is oxygen level-dependent.[54] Although oxygen dependency may act as another confounding factor for quantifying the NOE CEST contrast at −1.6 ppm, it may also be leveraged for probing intrarenal hypoxia, which is a common phenomenon in the medullae of the diseased kidneys.[55,56] The NOE at −1.6 ppm significantly decreased with the onset of injury from AA infusion, whereas the cisplatin group only showed minimal changes in the IM + P. Similar to NOE at −3.5 ppm, it is expected that the decrease is arising from the disruption of the tubular cell membrane as confirmed by the histology. Although the origin of the NOE at −1.6 ppm contrast should be further elucidated, the results indicate this contrast can be a useful imaging marker for observing renal diseases.

Several factors should be considered to implement our approach in the clinics. The saturation scheme, especially for the pools that have offset frequencies close to water such as urea and NOE at −1.6 ppm, should be reoptimized at the clinical field strength. Because the spectral resolution decreases at a lower B_0 field strength, it is crucial to minimize the direct water saturation so that urea and

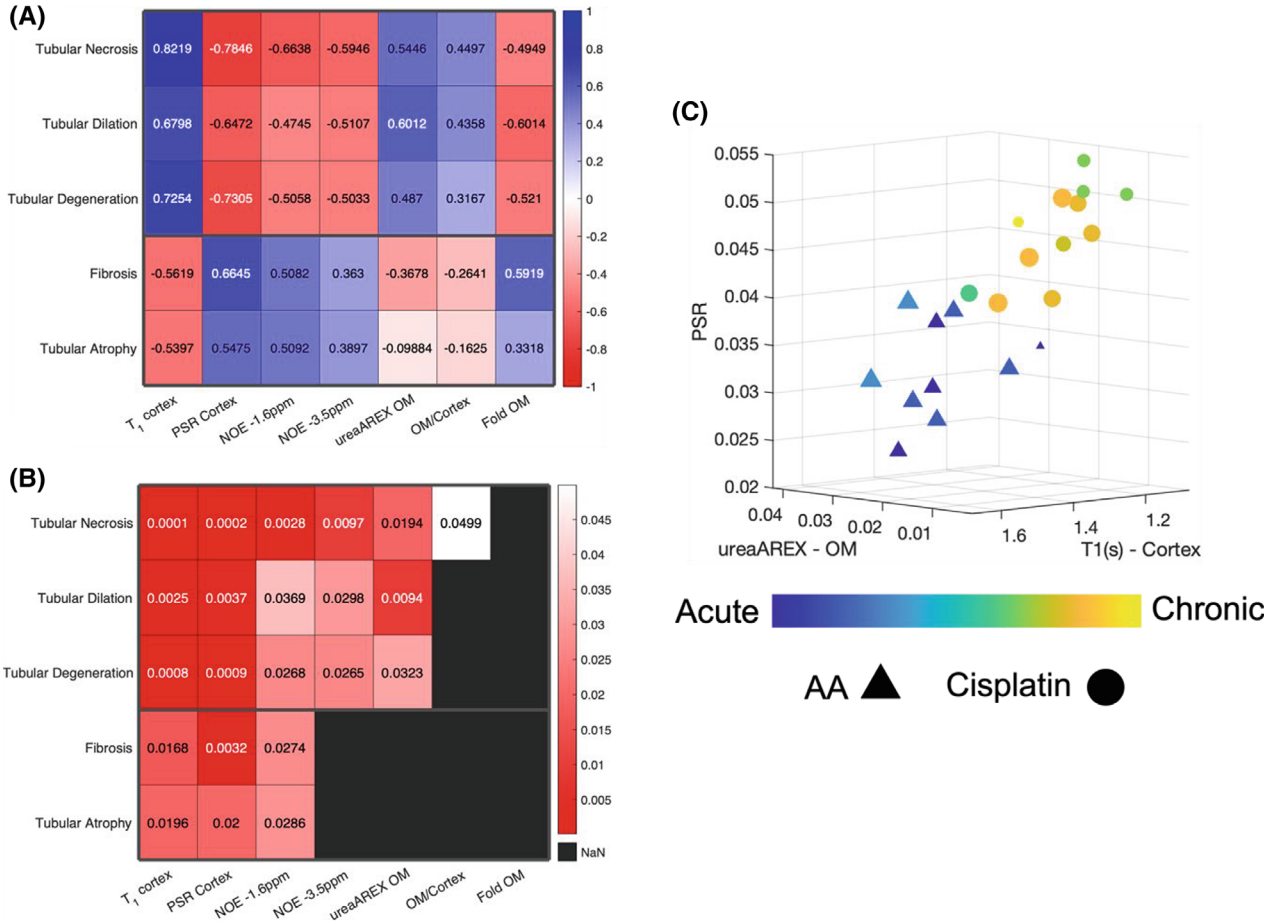

FIGURE 7 Correlation of CEST and quantitative magnetization transfer (qMT) parameters to histology. Spearman correlation coefficients (A) and *p*-values (B) are shown. T_1, pool-size ratio (PSR), and nuclear Overhauser enhancement (NOE) at −1.6 ppm in the cortex are sensitive to both acute and chronic injuries, whereas NOE at −3.5 ppm and urea apparent exchange-dependent relaxation (AREX) in the outer medulla (OM) are sensitive only to acute injuries. T_1 of the cortex is positively correlated to acute injuries and negatively to chronic ones, whereas PSR and NOE at −1.6 ppm show the opposite correlations. Black boxes in (B) indicate correlations that do not show statistical significance ($p > 0.05$). (C) An example multiparametric analysis of renal injuries. The combination of PSR, T_1 of the cortex, and urea AREX at the OM well distinguishes acute and chronic injuries. The size of data points indicates the overall severity of injuries as measured by cumulative layout shift (CLS) histological scores

NOE CEST contrasts are not affected. Second, the acquisition of full Z-spectra should be accelerated to reduce the total scan time to the level that is feasible in the clinics. A Z-spectrum was composed of 59 offset frequencies in this study, which took around 25 min. Furthermore, acquiring other parametric maps such as T_1, B_0, and B_1 maps were also needed for correction purposes, further elongating the total scan time. Several acceleration methods such as compressed sensing algorithms and deep learning approaches may be considered to overcome this issue.[57–60]

Some limitations of this study should be noted. Although we aimed to observe the progression of renal injuries toward the chronic end using the cisplatin model, histological findings suggest insufficient fibrosis development compared to previous mouse CKD models. Longer experiment timelines using mouse strains that are more vulnerable to cisplatin-induced injuries may induce more chronic injuries and enable investigation of how CEST and qMT parameters change at the chronic end of the spectrum of renal diseases.[61–64] In the CEST MRI perspective, the measurement of urea and NOE AREX is affected by the exchange rate of the target protons, which in turn is a function of the pH of the surrounding environment. Similar to T_1 times, intrarenal pH varies depending on the anatomical regions in the kidney, ranging from 7.0 to 6.6 from the cortex to IM + P.[24] Furthermore, it is likely that the pH of each kidney subregions change over disease progression.[22] Previous iopamidol CEST studies on mouse AKI models showed increasing pH levels from 6.7 to 7.3 in the kidneys with disease progression.[65,66] This spatiotemporal change of pH should alter the exchange rate of the target protons and affect the CEST contrast,

resulting in inaccurate estimation of renal function and tissue integrity loss. Several technical methods, such as numerical fitting of Bloch equations with different saturation times and saturation powers (QUEST/QUESP) and omega plot analysis, can be considered for correcting the pH effects by quantifying exchange rates.[67–69] Other metabolites in the kidneys that also possess exchangeable protons resonating at 1 ppm offset frequency, such as myo-inositol, alanine, and glucose may also confound the urea CEST quantification.[70] Because urea has a slow exchange rate, exchange rate-filter-based methods such as variable delay multi-pulse and frequency-labeled exchange transfer methods may be useful to isolate urea CEST contrast from other fast exchanging protons.[71–73]

5 | CONCLUSIONS

In this study, we designed a multiparametric CEST and qMT approach and tested its capability of quantitatively differentiating distinct nephropathies. Cisplatin and AA-induced nephropathy models showed different patterns of CEST and qMT parameter changes that reflect histological changes, indicating the potential of our approach for noninvasively characterizing the pathophysiology of different renal diseases.

ACKNOWLEDGMENTS

This study was supported by the National Institutes of Health (1R01HL28592, UH2EB028908, UH3EB028908) and the American Heart Association (19TPA34850040). The authors are also grateful to the Comparative Pathology Laboratory at the University of California, Davis for consultation on histology.

ORCID

Soo Hyun Shin https://orcid.org/0000-0003-1875-2908
Moriel H. Vandsburger https://orcid.org/0000-0003-4052-205X

REFERENCES

1. Ostermann M, Joannidis M. Acute kidney injury 2016: diagnosis and diagnostic workup. *Crit Care*. 2016;20:1-13.
2. Webster AC, Nagler EV, Morton RL, Masson P. Chronic kidney disease. *Lancet*. 2017;389:1238-1252.
3. Stevens LA, Coresh J, Greene T, Levey AS. Assessing kidney function—measured and estimated glomerular filtration rate. *N Engl J Med*. 2006;354:2473-2483.
4. Chawla LS, Eggers PW, Star RA, Kimmel PL. Acute kidney injury and chronic kidney disease as interconnected syndromes. *N Engl J Med*. 2014;371:58-66. doi:10.1056/nejmra1214243
5. Williams WW, Taheri D, Tolkoff-rubin N, Colvin RB. Clinical role of the renal transplant biopsy. *Nat Rev Nephrol*. 2012;8:110-121.
6. Morozumi K, Takeda A, Otsuka Y, Horike K, Gotoh N, Watarai Y. Recurrent glomerular disease after kidney transplantation: an update of selected areas and the impact of protocol biopsy. *Nephrology (Carlton)*. 2014;19:6-10. doi:10.1111/nep.12255
7. Chawla LS, Kimmel PL. Acute kidney injury and chronic kidney disease: an integrated clinical syndrome. *Kidney Int*. 2012;82:516-524. doi:10.1038/ki.2012.208
8. Gameiro J, Marques F, Lopes JA. Long-term consequences of acute kidney injury: a narrative review. *Clin Kidney J*. 2021;14:789-804. doi:10.1093/ckj/sfaa177
9. O'Neill WC. Renal relevant radiology: use of ultrasound in kidney disease and nephrology procedures. *Clin J Am Soc Nephrol*. 2014;9:373-381.
10. Sharfuddin A. Renal relevant radiology: imaging in kidney transplantation. *Clin J Am Soc Nephrol*. 2014;9:416-429.
11. Rha SE, Byun JY, Jung SE, et al. The renal sinus: pathologic spectrum and multimodality imaging approach. *Radiographics*. 2004;24:S117-S131.
12. Das CJ, Ahmad Z, Sharma S, Gupta AK. Multimodality imaging of renal inflammatory lesions. *World J Radiol*. 2014;6:865-873.
13. Ebrahimi B, Textor SC, Lerman LO. Renal relevant radiology: renal functional magnetic resonance imaging. *Clin J Am Soc Nephrol*. 2014;9:395-405.
14. Grenier N, Merville P, Combe C. Radiologic imaging of the renal parenchyma structure and function. *Nat Rev Nephrol*. 2016;12:348-359.
15. Davenport MS, Khalatbari S, Dillman JR, Cohan RH, Caoili EM, Ellis JH. Contrast material-induced nephrotoxicity and intravenous low-osmolality iodinated contrast material. *Radiology*. 2013;267:94-105. doi:10.1148/radiol.12121394
16. Marckmann P, Skov L, Rossen K, et al. Nephrogenic systemic fibrosis: suspected causative role of gadodiamide used for contrast-enhanced magnetic resonance imaging. *J Am Soc Nephrol*. 2006;17:2359-2362. doi:10.1681/ASN.2006060601
17. Liu G, Song X, Chan KWY, Mcmahon MT. Nuts and bolts of CEST MR imaging. *NMR Biomed* 2013;26(7):810828. doi:10.1002/nbm.2899, 810-828.
18. Knutsson L, Xu J, Ahlgren A, van Zijl PCM. CEST, ASL, and magnetization transfer contrast: how similar pulse sequences detect different phenomena. *Magn Reson Med*. 2018;80:1320-1340.
19. Vinogradov E, Sherry AD, Lenkinski RE. CEST: from basic principles to applications, challenges and opportunities. *J Magn Reson*. 2013;229:155-172.
20. Shin SH, Wendland MF, Zhang B, Tran A, Tang A, Vandsburger MH. Noninvasive imaging of renal urea handling by CEST-MRI. *Magn Reson Med*. 2020;83:1034-1044.
21. Shin SH, Wendland MF, Vandsburger MH. Delayed urea differential enhancement CEST (dudeCEST)-MRI with T1 correction for monitoring renal urea handling. *Magn Reson Med*. 2021;85:2791-2804. doi:10.1002/mrm.28583
22. Pavuluri KD, Manoli I, Pass A, et al. Noninvasive monitoring of chronic kidney disease using pH and perfusion imaging. *Sci Adv*. 2019;5:1-11.
23. Longo DL, Dastru W, Digilio G, et al. Iopamidol as a responsive MRI-chemical exchange saturation transfer contrast agent for pH mapping of kidneys: in vivo studies in mice at 7 T. *Magn Reson Med*. 2011;65:202-211.

24. Wu Y, Zhou IY, Igarashi T, Longo DL, Aime S, Sun PZ. A generalized ratiometric chemical exchange saturation transfer (CEST) MRI approach for mapping renal pH using iopamidol. *Magn Reson Med*. 2018;79:1553-1558.
25. Moon BF, Jones KM, Chen LQ, et al. A comparison of iopromide and iopamidol, two acidoCEST MRI contrast media that measure tumor extracellular pH. *Contrast Media Mol Imaging*. 2015;10:446-455.
26. Yang B, Bankir L. Urea and urine concentrating ability: new insights from studies in mice. *Am J Physiol Ren Physiol*. 2005;288:F881-F896.
27. Bankir L, Chen K, Yang B. Lack of UT-B in vasa recta and red blood cells prevents urea-induced improvement of urinary concentrating ability. *Am J Physiol Renal Physiol*. 2004;286:F144-F151.
28. Bankir L, Bouby N, Trinh-Trang-Tan MM, Ahloulay M, Promeneur D. Direct and indirect cost of urea excretion. *Kidney Int*. 1996;49:1598-1607.
29. Schmidt C, Höcherl K, Bucher M. Cytokine-mediated regulation of urea transporters during experimental endotoxemia. *Am J Physiol Renal Physiol*. 2007;292:F1479-F1489.
30. Zhang X, Laustsen C, Bertelsen LB, et al. Diabetes induced renal urea transport alterations assessed with 3D hyperpolarized 13 C, 15 N-urea. *Magn Reson Med*. 2016;77:1650-1655.
31. Zaiss M, Windschuh J, Paech D, et al. Relaxation-compensated CEST-MRI of the human brain at 7T: unbiased insight into NOE and amide signal changes in human glioblastoma. *NeuroImage*. 2015;112:180-188.
32. Jones CK, Huang A, Xu J, et al. Nuclear Overhauser enhancement (NOE) imaging in the human brain at 7T. *NeuroImage*. 2013;77:114-124. doi:10.1016/j.neuroimage.2013.03.047
33. Liu J, Han Z, Chen G, et al. CEST MRI of sepsis-induced acute kidney injury. *NMR Biomed*. 2018;31:e3942. doi:10.1002/nbm.3942
34. Wang F, Kopylov D, Zu Z, et al. Mapping murine diabetic kidney disease using chemical exchange saturation transfer MRI. *Magn Reson Med*. 2015;76:1531-1541. doi:10.1002/mrm.26045
35. Sled JG, Pike GB. Quantitative interpretation of magnetization transfer in spoiled gradient Echo MRI sequences. *J Magn Reson*. 2000;145:24-36. doi:10.1006/jmre.2000.2059
36. Sled JG, Bruce PG. Quantitative imaging of magnetization transfer exchange and relaxation properties in vivo using MRI. *Magn Reson Med*. 2001;46:923-931. doi:10.1002/mrm.1278
37. Wang F, Katagiri D, Li K, et al. Assessment of renal fibrosis in murine diabetic nephropathy using quantitative magnetization transfer MRI. *Magn Reson Med*. 2018;80:2655-2669. doi:10.1002/mrm.27231
38. Wang F, Wang S, Zhang Y, et al. Noninvasive quantitative magnetization transfer MRI reveals tubulointerstitial fibrosis in murine kidney. *NMR Biomed*. 2019;32:1-13. doi:10.1002/nbm.4128
39. Desmond KL, Moosvi F, Stanisz GJ. Mapping of amide, amine, and aliphatic peaks in the CEST spectra of murine xenografts at 7T. *Magn Reson Med*. 2014;71:1841-1853.
40. Zaiss M, Xu J, Goerke S, et al. Inverse Z-spectrum analysis for spillover-, MT-, and T1-corrected steady-state pulsed CEST-MRI—application to pH-weighted MRI of acute stroke. *NMR Biomed*. 2014;27:240-252.
41. Ramani A, Dalton C, Miller DH, Tofts PS, Barker GJ. Precise estimate of fundamental in-vivo MT parameters in human brain in clinically feasible times. *Magn Reson Imaging*. 2002;20:721-731. doi:10.1016/S0730-725X(02)00598-2
42. Baudoux TER, Pozdzik AA, Arlt VM, et al. Probenecid prevents acute tubular necrosis in a mouse model of aristolochic acid nephropathy. *Kidney Int*. 2012;82:1105-1113.
43. Hansen ESS, Stewart NJ, Wild JM, Stødkilde-Jørgensen H, Laustsen C. Hyperpolarized ^{13}C,$^{15}N_2$-Urea MRI for assessment of the urea gradient in the porcine kidney. *Magn Reson Med*. 2016;76:1895-1899. doi:10.1002/mrm.26483
44. Gomez H, Ince C, De Backer D, et al. A unified theory of sepsis-induced acute kidney injury: inflammation, microcirculatory dysfunction, bioenergetics, and the tubular cell adaptation to injury. *Shock*. 2014;41:3-11. doi:10.1097/SHK.0000000000000052
45. Cai K, Xu HN, Singh A, et al. Breast cancer redox heterogeneity detectable with chemical exchange saturation transfer (CEST) MRI. *Mol Imaging Biol*. 2014;16:670-679. doi:10.1007/s11307-014-0739-y
46. Jiang K, Ferguson CM, Ebrahimi B, et al. Noninvasive assessment of renal fibrosis with magnetization transfer MR imaging: validation and evaluation in murine renal artery stenosis. *Radiology*. 2017;283:77-86. doi:10.1148/radiol.2016160566
47. Jiang K, Ferguson CM, Woollard JR, Zhu X, Lerman LO. Magnetization transfer magnetic resonance imaging noninvasively detects renal fibrosis in swine atherosclerotic renal artery stenosis at 3.0T. *Investig Radiol*. 2017;52:686-692. doi:10.1097/RLI.0000000000000390
48. Jiang K, Fang Y, Ferguson CM, et al. Quantitative magnetization transfer detects renal fibrosis in murine kidneys with renal artery stenosis. *J Magn Reson Imaging*. 2021;53:884-893. doi:10.1002/jmri.27370
49. Zhang XY, Wang F, Afzal A, et al. A new NOE-mediated MT signal at around −1.6 ppm for detecting ischemic stroke in rat brain. *Magn Reson Imaging*. 2016;34:1100-1106.
50. Zu Z. Ratiometric NOE(−1.6) contrast in brain tumors. *NMR Biomed*. 2018;31:1-10. doi:10.1002/nbm.4017
51. Cui J, Zhao Y, Wang F, Gochberg DF, Zu Z. Contribution of blood to nuclear Overhauser effect at −1.6 ppm. *Magn Reson Med*. 2022;87:409-416. doi:10.1002/mrm.28973
52. Chang YC, Liu HQ, Chang JH, Chang YY, Lin EC. Role of the cholesterol hydroxyl group in the chemical exchange saturation transfer signal at −1.6 ppm. *NMR Biomed*. 2020;33:1-8. doi:10.1002/nbm.4356
53. Zhang XY, Wang F, Jin T, et al. MR imaging of a novel NOE-mediated magnetization transfer with water in rat brain at 9.4T. *Magn Reson Med*. 2017;78:588-597. doi:10.1002/mrm.26396
54. Zu Z. Toward more reliable measurements of NOE effects in CEST spectra at around −1.6 ppm (NOE (−1.6)) in rat brain. *Magn Reson Med*. 2019;81:208-219.
55. Eckardt KU, Bernhardt WM, Weidemann A, et al. Role of hypoxia in the pathogenesis of renal disease. *Kidney Int*. 2005;68:46-51. doi:10.1111/j.1523-1755.2005.09909.x
56. Tanaka S, Tanaka T, Nangaku M. Hypoxia as a key player in the AKI-to-CKD transition. *Am J Physiol Renal Physiol*. 2014;307:F1187-F1195. doi:10.1152/ajprenal.00425.2014
57. Lam B, Wendland M, Godines K, Shin SH, Vandsburger M. Accelerated multi-target chemical exchange saturation transfer magnetic resonance imaging of the mouse heart. *Phys Med Biol*. 2021;66:145016.

58. Chen L, Schär M, Chan KWY, et al. In vivo imaging of phosphocreatine with artificial neural networks. *Nat Commun*. 2020;11:1-10.
59. Perlman O, Ito H, Herz K, et al. Deep learning of magnetic resonance fingerprints for the quantitative imaging of apoptosis following oncolytic virotherapy. *Nat Biomed Eng*. 2022;6:648-657.
60. Perlman O, Zhu B, Zaiss M, Rosen MS, Farrar CT. An end-to-end AI-based framework for automated discovery of rapid CEST/MT MRI acquisition protocols and molecular parameter quantification (AutoCEST). *Magn Reson Med*. 2022;87:2792-2810.
61. Sharp CN, Doll MA, Dupre TV, et al. Repeated administration of low-dose cisplatin in mice induces fibrosis. *Am J Physiol*. 2016;310:F560-F568. doi:10.1152/ajprenal.00512.2015
62. Sharp CN, Siskind LJ. Developing better mouse models to study cisplatin-induced kidney injury. *Am J Physiol*. 2017;313:F835-F841. doi:10.1152/ajprenal.00285.2017
63. Sharp CN, Doll MA, Megyesi J, Oropilla GB, Beverly LJ, Siskind LJ. Subclinical kidney injury induced by repeated cisplatin administration results in progressive chronic kidney disease. *Am J Physiol Renal Physiol*. 2018;315:F161-F172. doi:10.1152/ajprenal.00636.2017
64. Sears SM, Sharp CN, Krueger A, et al. C57BL/6 mice require a higher dose of cisplatin to induce renal fibrosis and CCL2 correlates with cisplatin-induced kidney injury. *Am J Physiol Renal Physiol*. 2020;319:F674-F685. doi:10.1152/ajprenal.00196.2020
65. Longo DL, Cutrin JC, Michelotti F, Irrera P, Aime S. Noninvasive evaluation of renal pH homeostasis after ischemia reperfusion injury by CEST-MRI. *NMR Biomed*. 2017;30:1-8.
66. Longo DL, Busato A, Lanzardo S, Antico F, Aime S. Imaging the pH evolution of an acute kidney injury model by means of iopamidol, a MRI-CEST pH-responsive contrast agent. *Magn Reson Med*. 2013;70:859-864.
67. McMahon MT, Gilad AA, Zhou J, Sun PZ, Bulte JWM, Van Zijl PCM. Quantifying exchange rates in chemical exchange saturation transfer agents using the saturation time and saturation power dependencies of the magnetization transfer effect on the magnetic resonance imaging signal (QUEST and QUESP): pH calibration for poly. *Magn Reson Med*. 2006;55:836-847. doi:10.1002/mrm.20818
68. Dixon WT, Ren J, Lubag AJM, et al. A concentration-independent method to measure exchange rates in PARACEST agents. *Magn Reson Med*. 2010;63:625-632.
69. Meissner JE, Goerke S, Rerich E, et al. Quantitative pulsed CEST-MRI using Ω-plots. *NMR Biomed*. 2015;28:1196-1208.
70. Stabinska J, Neudecker P, Ljimani A, Wittsack HJ, Lanzman RS, Müller-Lutz A. Proton exchange in aqueous urea solutions measured by water-exchange (WEX) NMR spectroscopy and chemical exchange saturation transfer (CEST) imaging in vitro. *Magn Reson Med*. 2019;82:935-947.
71. Xu J, Yadav NN, Bar-shir A, et al. Variable delay multi-pulse train for fast chemical exchange saturation transfer and relayed-nuclear Overhauser enhancement MRI. *Magn Reson Med*. 2014;71:1798-1812.
72. Chen L, Xu X, Zeng H, et al. Separating fast and slow exchange transfer and magnetization transfer using off-resonance variable-delay multiple-pulse (VDMP) MRI. *Magn Reson Med*. 2018;80:1568-1576.
73. Yadav NN, Jones CK, Xu J, et al. Detection of rapidly exchanging compounds using on-resonance frequency-labeled exchange (FLEX) transfer. *Magn Reson Med*. 2012;68:1048-1055. doi:10.1002/mrm.24420

How to cite this article: Shin SH, Wendland MF, Wang J, Velasquez M, Vandsburger MH. Noninvasively differentiating acute and chronic nephropathies via multiparametric urea-CEST, nuclear Overhauser enhancement-CEST, and quantitative magnetization transfer MRI. *Magn Reson Med*. 2023;89:774-786. doi:10.1002/mrm.29477